

THEORY AND MODELLING

Quasi-steady aerodynamic theory under-predicts glide performance in flying snakes

Isaac J. Yeaton^{1,2}, Shane D. Ross³, and John J. Socha¹**ABSTRACT**

Flying snakes (genus *Chrysopelea*) glide without the use of wings. Instead, they splay their ribs and undulate through the air. A snake's ability to glide depends on how well its morphing wing-body produces lift and drag forces. However, previous kinematics experiments under-resolved the body, making it impossible to estimate the aerodynamic load on the animal or to quantify the different wing configurations throughout the glide. Here, we present new kinematic analyses of a previous glide experiment, and use the results to test a theoretical model of flying snake aerodynamics using previously measured lift and drag coefficients to estimate the aerodynamic forces. This analysis is enabled by new measurements of the center of mass motion based on experimental data. We find that quasi-steady aerodynamic theory under-predicts lift by 35% and over-predicts drag by 40%. We also quantify the relative spacing of the body as the snake translates through the air. In steep glides, the body is generally not positioned to experience tandem effects from wake interaction during the glide. These results suggest that unsteady 3D effects, with appreciable force enhancement, are important for snake flight. Future work can use the kinematics data presented herein to form test conditions for physical modeling, as well as computational studies to understand unsteady fluid dynamic effects on snake flight.

KEYWORDS: gliding, snake, undulation, aerodynamics**INTRODUCTION**

Animal flight requires producing and controlling aerodynamic lift and drag forces via neuromuscular control and/or specialized morphology. Flapping fliers use paired beating wings, while most vertebrate gliders deploy pairs of stretched skin between limbs (Byrnes et al., 2008; Bahlman et al., 2013; Khandelwal and Hedrick, 2022), extendable ribs (McGuire, 2003; McGuire and Dudley, 2005), webbed feet (McCay, 2001), or modified fins (Park and Choi, 2010; O'Dor et al., 2013). By contrast, flying snakes flatten their bodies and undulate through the air, turning the whole animal into an 'S'-shaped morphing wing-body (Socha, 2002). The wing-body changes configuration continuously throughout the

glide as the body forms straight segments connected by tight lateral bends that travel posteriorly (figure 1D) (Socha et al., 2005). The snake's aerial undulation is composed of horizontal and vertical waves which are 90° out of phase and whose frequencies differ by a factor of two (Yeaton et al., 2020). While airborne, the posture of the body is never symmetric about any axis, which has functional implications for force production and balance, and distinguishes flying snakes from most other flapping flyers or gliders (Khandelwal et al., 2023).

A fundamental component to snake flight is how effective the wing-body is at producing lift and drag forces, and how these forces change as the animal accelerates and the glide shallows (Socha et al., 2015). Understanding lift and drag production requires knowing the detailed kinematics of the morphing wing, as well as the lift and drag characteristics of the wing at each configuration. Given the orientation of the wing-body and the lift and drag coefficients of the cross-section, first-order approximations of the lift and drag forces can be calculated using the quasi-steady assumption (Ellington, 1984; Yeaton et al., 2020).

The quasi-steady assumption states that the forces acting on a wing are a function of its instantaneous speed and orientation to the flow; its acceleration and the time history of the flow are not considered. The validity of quasi-steady theory can be checked by examining if the resultant aerodynamic force matches the center of mass acceleration of the animal. Although the quasi-steady assumption has proved insufficient to explain force production during flapping flight of insects and vertebrates (Hedenström et al., 2007; Warrick et al., 2005; Videler et al., 2004; Ellington et al., 1996; Muijres et al., 2008; Maxworthy, 1981; Dudley and Ellington, 1990; Dickinson et al., 1999; Chin and Lentink, 2016), it has not been tested explicitly for animal gliders (*sensu stricto*) with their nominally static body postures (Socha, 2011; Socha et al., 2015). Despite flying snakes displaying large postural changes involved in aerial undulation, a previous study found that undulation frequency was not significantly correlated to any glide performance variables, suggesting that undulation itself has a minor role in aerodynamic force production and that quasi-steady theory could be applicable (Socha and LaBarbera, 2005). Additionally, the fast forward speed compared to the relatively slow speed of undulation, quantified as the advance ratio, also suggests that quasi-steady theory might be applicable (Holden et al., 2014). However, the precise aerodynamic forces produced during snake flight have never been calculated because the detailed wing-body kinematics and the center of mass trajectory were unknown.

A quasi-steady analysis requires known lift and drag coefficients for the flyer of interest. The lift and drag characteristics of the 2D cross-sectional shape of *C. paradisi* have been studied previously using load cell measurements, particle image velocimetry, and computational fluid dynamics (Miklasz et al., 2010; Holden

¹Department of Mechanical Engineering, Virginia Tech, Blacksburg, VA 24061, USA

²Applied Physics Laboratory, Johns Hopkins University, Baltimore, Md 20723 USA

³Department of Aerospace and Ocean Engineering, Virginia Tech, Blacksburg, VA 24061, USA

Authors for correspondence: (jjsocha@vt.edu)

et al., 2014; Krishnan et al., 2014). The roughly triangular cross-section acts as a lifting bluff body (figures 1D and 2A), with the concave ventral surface and protruding lips serving to improve force production (Miklasz et al., 2010). The shape produces appreciable lift over a large range of angle of attack, with the lift-to-drag ratio peaking at an angle of attack of 35° (figure 2A). The profile has gentle stall characteristics, with drag increasing slowly after 35° . The cross-section is also effective at producing lift at high angles of attack, as the lift coefficient at 60° is roughly the same as at 15° . Additional physical modeling also determined that when two snake-like profiles are offset, there is a modification of the lift and drag through wake interaction effects (Miklasz et al., 2010). More recent physical modeling investigated such ‘tandem’ effects, finding appreciable lift-to-drag ratio changes for particular wing configurations of gap (horizontal spacing) and stagger (vertical spacing) that may be realizable during gliding (Jafari et al., 2021).

In addition to the lift and drag characteristics, quasi-steady theory requires knowledge of the body’s kinematics: the instantaneous wing configuration, its orientation to the flow, and each body segment’s motion. Previous kinematic measurements of snake flight recorded either three or five landmarks on the body (Socha, 2002; Socha et al., 2005; 2010). Although these data enabled a detailed center of mass trajectory analysis, the time-varying body posture and its orientation to the airflow had to be estimated from the horizontal body posture and glide angle. However, in a real flying snake, different sections of the body might experience different angles of attack, and portions of the body are swept relative to the airflow, which will affect the forces and moments acting on the body. Additionally, the out-of-plane bending of the body causes the snake’s wing-body to twist, thereby changing the local angle of attack (Yeaton et al., 2020). These complexities of the aerial snake made it impossible to estimate the locomotor forces from a few landmark points alone, and proved insufficient for guiding modeling studies. Additionally, the center of mass position, velocity, and acceleration could only be estimated, as the true configuration of the body was not known.

Here, we test the effectiveness of quasi-steady theory at approximating lift and drag forces along a flying snake’s body during gliding. To do so, we did two things: 1) We conducted a new analysis of three-dimensional kinematics data from our recent study (Yeaton et al., 2020). Specifically, we used 11–17 landmark points along the snake’s body to recover the snake’s time-varying body posture recorded in an experimental setting. This new analysis enabled us to estimate the center of mass position with high fidelity and subsequently calculate velocity and acceleration. Knowing the mass of the snake, we then used the center of mass acceleration to calculate the total time-varying aerodynamic force on the snake, which we take as the ‘true’ value. 2) Then, using as few assumptions as possible, we estimated the time-varying aerodynamic force produced across the entire body as predicted by quasi-steady theory. To do so, we used the 3D kinematics to define the local wing orientation, and calculated quasi-steady lift and drag forces using the previously measured 2D force coefficients, the blade element method, and simple sweep theory. This calculation of forces is a sum of infinitesimal elements, which analogizes the snake as collection of particles that connect with one another, but does not behave as a rigid body. We then tested the quasi-steady assumption by comparing the absolute errors between the center of mass force (‘true’) and the estimated theoretical aerodynamic force (‘model’). This study provides the first detailed analysis of the total aerodynamic load on flying snakes during gliding. Additionally, we use

the kinematics data to estimate how Reynolds number, angle of attack, and sweep angle vary along the body, which can be used to inform future physical and computational modeling of snake flight.

METHODS

New analyses of snake kinematics

This study newly analyzes 3D kinematics data from an experiment originally presented in Yeaton et al. (2020). The main focus of that paper was to develop a quasi-steady analysis of gliding to examine the role of aerial undulation on gliding. Data related to undulation were presented therein, and the remainder of the un-analyzed kinematics data are addressed in the current study. A total of 43 glide trials from 7 snakes of the species *Chrysopelea paradisi* are presented here. We refer the reader to the previous paper for the full details of the experiment; for convenience, a brief summary is provided below.

We recorded the position of between 11 and 17 infrared tape markers placed along the dorsal surface of flying snakes using a 23-camera motion capture system with a sampling rate of 179 Hz. Experiments were conducted in ‘The Cube’, a four-story-tall black-box theatre located in the Moss Arts Center at Virginia Tech, modified for use as a large indoor glide arena (figure 1A-C) under IACUC protocol #15-034. Snakes were allowed to jump and glide under their own volition from a height of 8.3 m. From the landmark points, we exported the marker trajectories and filled gaps using Kalman filters. We then smoothed the marker time series using two passes of a 2nd-order Butterworth filter, with cutoff frequencies selected separately for each coordinate time series for each marker (Winter, 2009); these values ranged from 7–17 Hz, which are greater than the nominal undulation frequencies observed in gliding snakes ($\approx 1-2$ Hz).

From the filtered marker time series, we fit cubic splines to form a continuous representation of the body at each moment in time (figure 3A,B). The spline defines the position of each segment k of the body, $\vec{r}_k^I(t) = (x_k(t), y_k(t), z_k(t))$, relative to the inertial frame. We calculated the velocity and acceleration of each location along the body in the inertial frame using finite differences,

$$\vec{v}_k^I(t) = \frac{\vec{r}_k^I(t + \Delta t) - \vec{r}_k^I(t - \Delta t)}{2\Delta t} \quad (1)$$

$$\vec{a}_k^I(t) = \frac{\vec{r}_k^I(t + \Delta t) - 2\vec{r}_k^I(t) + \vec{r}_k^I(t - \Delta t)}{\Delta t^2} \quad (2)$$

with second-order accurate forward and backward differences used at the beginning and end of each time series. We then superimposed the average mass distribution, measured from snake sectioning (Yeaton et al., 2020), onto the spline and calculated the center of mass in the inertial frame as,

$$\vec{R}_o^I(t) = \frac{1}{M} \sum_k m_k \vec{r}_k^I(t), \quad (3)$$

where $\vec{R}_o^I(t)$ is the center of mass, m_k is the mass of segment k of the body (figure 3E), and M is the total mass. The center of mass position was then filtered using a Butterworth filter as above, and the center of mass velocity and acceleration were calculated using finite differences.

The center of mass trajectory was then iteratively rotated from the inertial frame into a straightened frame such that the glide path aligns with the vertical YZ plane while preserving the total arc-length displacement of the center of mass. The kinematic variables

were rotated about the Z axis into the straightened frame by the yaw angle, ψ , calculated using the X and Y velocities of the center of mass, as,

$$\psi = -\tan^{-1}(\dot{R}_{o,X}/\dot{R}_{o,Y}), \quad (4)$$

where $\dot{\vec{R}}_o^I(t) = (\dot{R}_{o,X}, \dot{R}_{o,Y}, \dot{R}_{o,Z})$ is the center of mass inertial velocity. The glide angle, γ , was calculated from the straightened frame center of mass velocity as,

$$\gamma = -\tan^{-1}(\dot{R}_{o,Z}/\dot{R}_{o,Y}), \quad (5)$$

which is the angle of the center of mass velocity down from the horizontal plane.

Center of mass motion

The center of mass motion was newly analyzed by considering the trajectories from the overhead view in the inertial frame (X and Y), as well as the side view in the straightened trajectory frame (Y and Z). The trajectories were also analyzed using velocity polar diagrams, which encode how the forward and vertical velocity change during the glide. These diagrams also encode the glide angle and different phases of gliding (ballistic, shallowing, equilibrium), which can be related to the angle-of-attack dependent lift and drag characteristics of the glider (Yeaton et al., 2017). The velocities, and therefore the entire diagram, can be non-dimensionalized and rescaled using an animal-specific characteristic velocity scale, v^* , given by,

$$v^* = \sqrt{\frac{2W_S}{\rho}}, \quad (6)$$

where W_S is the wing loading and ρ is the air density. Physically, the velocity scale, v^* , is equivalent to the terminal velocity if the drag coefficient were 1. The velocities are scaled as,

$$\hat{v} = \frac{v}{v^*}. \quad (7)$$

The non-dimensionalization and rescaling enables us to compare trajectories from different individuals with different sizes.

Reconstructing the wing-body orientation

The wing orientation of the snake's body was reconstructed by overlaying an airfoil coordinate system onto the spline (figure 3C,D). The airfoil coordinate system, denoted as $\{\hat{T}, \hat{C}, \hat{B}\}$, allows us to calculate the orientation of each local body segment relative to the flow and its resulting aerodynamic forces. To define the airfoil coordinate system, we used the local unit tangent vector, \hat{T} , of the spline and the inertial \hat{Z} direction. The unit tangent vector is locally tangent to the body at arc-length location s and time t and points posteriorly down the body from the head to the vent and is defined from the spline only. The local chord-line direction, denoted as \hat{C} , was assumed to be along a horizontal direction along the cross-product $\hat{Z} \times \hat{T}$. Lastly, the right-handed coordinate system was completed by a direction which locally points up through the backbone of the animal, denoted as \hat{B} . The

airfoil coordinate system is given by,

$$\hat{T}(s, t) = \left\| \frac{\partial \vec{r}^I(s, t)}{\partial s} \right\|, \quad (8)$$

$$\hat{C}(s, t) = \frac{\hat{Z} \times \hat{T}(s, t)}{\|\hat{Z} \times \hat{T}(s, t)\|}, \quad (9)$$

$$\hat{B}(s, t) = \hat{T}(s, t) \times \hat{C}(s, t), \quad (10)$$

where s is the arc-length coordinate and t is time. As mentioned previously, we defined $\hat{C}(s, t)$ such that it lies within the horizontal plane. We tried to define \hat{C} using other assumptions about minimal twisting of the snake, but visually the results did not match observed photographic and video footage of the glides. We note that using our approximation of $\hat{C}(s, t)$, the airfoil coordinate system twists depending on the local orientation of the body.

To reconstruct the time-varying three-dimensional body, we rotated the previously determined snake airfoil segment (Socha, 2011) to lie within the local \hat{C} - \hat{B} plane at each position along the body. The segment is then scaled to a specified width (which is also the chord length, $c(s)$) based on its arc-length distance along the body, s (figure 3F). Qualitatively, the resulting wing-body model is visually very similar to the observed body while gliding.

Lift and drag forces

Lift and drag forces were calculated using the blade element method and simple sweep theory, along with previously measured quasi-steady lift and drag coefficients from (Holden et al., 2014). Each location along the body was treated as aerodynamically independent (e.g., no wake-interaction effects) and the lift and drag forces were calculated as,

$$\vec{f}_L = \frac{\rho U_{\perp}^2}{2} \cdot c(s) \cdot C_L(\alpha, Re) \cdot \hat{L}, \quad (11)$$

$$\vec{f}_D = \frac{\rho U_{\perp}^2}{2} \cdot c(s) \cdot C_D(\alpha, Re) \cdot \hat{D}, \quad (12)$$

where \vec{f}_L and \vec{f}_D are the lift and drag force per unit length, respectively, ρ is the air density, U_{\perp} is the velocity locally perpendicular to the body, $c(s)$ is the measured chord length as it varies along the body, C_L and C_D are the lift and drag coefficients (figure 2A) as functions of angle-of-attack α and Reynolds number $Re = Uc/\nu$, where U is the total velocity magnitude, and \hat{L} and \hat{D} are described below. The total aerodynamic force that acts at the center of mass is calculated by integrating the lift and drag forces, which vary along the body and with time.

Simple sweep theory was used to calculate forces on the curved sections of the body. Only the velocity component that is locally perpendicular to the body was used to calculate the forces, which enabled us to use previously measured lift and drag coefficients for the snake body cross-section with a sweep angle of zero degrees. The local velocity, $\vec{R}(s, t)$, was projected into the $\hat{C}(s, t)$ - $\hat{B}(s, t)$ plane such that it is locally normal to the body as follows,

$$\dot{\vec{R}}_T = (\dot{\vec{R}} \cdot \hat{T})\hat{T}, \quad (13)$$

$$\dot{\vec{R}}_{CB} = \dot{\vec{R}} - \dot{\vec{R}}_T, \quad (14)$$

$$U_{\parallel} = \left\| \dot{\vec{R}}_T \right\|, \quad (15)$$

$$U_{\perp} = \left\| \dot{\vec{R}}_{CB} \right\|, \quad (16)$$

where the subscripts indicate along which direction the velocity lies. The angle of attack, α , is the angle between the perpendicular velocity and the chord-line direction, and is given by,

$$\alpha(s, t) = \cos^{-1} \left(\frac{\dot{\vec{R}}_{CB} \cdot \hat{C}}{U_{\perp}} \right). \quad (17)$$

The sweep angle, β , was calculated as the angle between the velocity within the plane of the bottom of the snake and the total velocity,

$$\beta(s, t) = \cos^{-1} \left(\frac{\dot{\vec{R}}_{TC} \cdot \hat{T}}{\|\dot{\vec{R}}_{TC}\|} \right) - \frac{\pi}{2}, \quad (18)$$

where $\dot{\vec{R}}_{TC} = \dot{\vec{R}} - \dot{\vec{R}}_B$ and $\dot{\vec{R}}_B = (\dot{\vec{R}} \cdot \hat{B})\hat{B}$. The shift of $\pi/2$ accounts for the above dot product as the angle between the tangent vector and the velocity, not the velocity and the chord-line direction.

The lift and drag coefficients are functions of both angle of attack and Reynolds number. The orientation of the drag vector, \hat{D} , is along the direction of the perpendicular velocity $\dot{\vec{R}}_{CB}$; the orientation of the lift vector, \hat{L} , is normal to both the tangent vector and drag vector. The force orientations are given by,

$$\hat{D} = -\dot{\vec{R}}_{CB}/U_{\perp}, \quad (19)$$

$$\hat{L} = \hat{T} \times \hat{D}. \quad (20)$$

The effect of simple sweep theory is to reduce the velocity in the force equations (11) and (12). We quantified this effect by taking the ratio of the forces with and without the simple sweep theory assumption. Because simple sweep theory only affects the velocity, this ratio is the fraction of the dynamic pressure due to the curved sections of the snake body. The dynamic pressure fraction reduces to,

$$q_f = \frac{U_{\perp}^2}{U^2}. \quad (21)$$

Aerodynamic force errors

We quantified the error of the quasi-steady force estimates by comparing the total aerodynamic force acting at the center of mass with the acceleration of the center of mass in the straightened frame. The translational equations of motion for the snake are,

$$\vec{F}_L + \vec{F}_D + m\vec{g} = m\ddot{\vec{R}}_o, \quad (22)$$

where m is the animal's mass, $\vec{g} = -g\hat{Z}$ is gravity, and $\ddot{\vec{R}}_o$ is the center of mass inertial acceleration. The total lift and drag forces acting at the center of mass, \vec{F}_L and \vec{F}_D , are,

$$\vec{F}_L = \int_0^L \vec{f}_L ds, \quad \vec{F}_D = \int_0^L \vec{f}_D ds, \quad \vec{F}_A = \vec{F}_L + \vec{F}_D, \quad (23)$$

where L is the length of the animal, \vec{F}_A is the total aerodynamic force, and \vec{f}_L and \vec{f}_D are the lift and drag per unit length, respectively. The translational equations of motion were normalized by the weight of each animal, mg , so that errors could be compared

across individuals. The weight term was then moved to the right-hand side of (22) to isolate the forces. This manipulation results in the normalized force equation,

$$\frac{\vec{F}_A}{mg} = \frac{\ddot{\vec{R}}_o}{g} + \hat{Z}. \quad (24)$$

The acceleration, $\ddot{\vec{R}}_o$, was measured experimentally while the aerodynamic force, \vec{F}_A , was from the quasi-steady aerodynamic model. In general, we do not expect these to be in agreement. That is, (24) will not hold. We quantify the aerodynamic force error as the non-dimensional vector,

$$\begin{aligned} \vec{\epsilon} &= \ddot{\vec{R}}_o - \vec{F}_A + \hat{Z}, \\ &= (\epsilon_X, \epsilon_Y, \epsilon_Z), \end{aligned} \quad (25)$$

where,

$$\begin{aligned} \epsilon_X &= \ddot{R}_{o,X} - \bar{F}_{A,X} \\ \epsilon_Y &= \ddot{R}_{o,Y} - \bar{F}_{A,Y} \\ \epsilon_Z &= \ddot{R}_{o,Z} - \bar{F}_{A,Z} + 1, \end{aligned} \quad (26)$$

where the bar indicates normalized forces ($\bar{F}_A = \vec{F}_A/(mg)$) and accelerations ($\ddot{R}_o = \ddot{\vec{R}}_o/g$), and the one in the ϵ_Z equation results from the gravitational acceleration. Because the errors were calculated in the straightened frame, ϵ_X is the lateral error of forces trying to move the center of mass away from the trajectory, ϵ_Y is the error contributing to forward motion, and ϵ_Z is the error in offsetting the animal's weight against gravity. Using the straightened frame allows us to compare errors consistently across trials. If instead we used the forces and acceleration in the inertial frame, the ϵ_X and ϵ_Y errors would not directly correlate to moving the animal away from the trajectory or for forward motion, but a less intuitive combination of the two.

For each trial, we compared the non-dimensional force errors as a function of the height of the animal's center of mass above the ground, as this proceeds with the progress of the glide in a manner which can be compared across all trials. Lastly, linear interpolation was used to interpolate the accelerations and forces such that each glide was sampled on a uniform height grid. This enabled us to calculate the averages and standard deviations of the forces, accelerations, and errors for each individual.

Quantifying differences between model and kinematics

In our aerodynamic analysis, we focused on quantifying the discrepancies between our model predictions and experimental observations. Specifically, we observed consistent deviations in the force estimates in the forward (ϵ_Y) and vertical (ϵ_Z) directions. Our model tended to overestimate drag force and underestimate lift force when compared to experimental data.

To quantify these discrepancies, we introduced time-varying multiplier factors $b_L(t)$ and $b_D(t)$ for the lift and drag forces, respectively. These factors represent how much we need to adjust the model's force estimates to align them with experimental observations, at each time t . Ideally, if the model perfectly matched the experiments, these multiplier factors would be 1, indicating no discrepancy.

We used a numerical minimization procedure to determine the precise values of these multiplier factors. At each time t , this process involved selecting $b_L(t)$ and $b_D(t)$ to minimize the modified center of mass error magnitude,

$$\epsilon'(t) = \|\ddot{\vec{R}}_o(t) - \vec{F}'_A(t) + \hat{Z}\|, \quad (27)$$

where the modified aerodynamic force is $\vec{F}'_A(t) = \vec{F}'_L(t) + \vec{F}'_D(t)$, where lift and drag are modified according to,

$$\vec{F}'_L(t) = b_L(t)\vec{F}_L(t), \quad \vec{F}'_D(t) = b_D(t)\vec{F}_D(t), \quad (28)$$

where the prime denotes the modified force.

Gap and stagger measurements

Gap and stagger are defined as the relative horizontal and vertical position of the downstream body segment relative to the upstream segment. To quantify the relative spacing of the body for possible wake interaction effects, we calculated the time-varying gap and stagger values of the snakes throughout the trajectory. Gap and stagger are calculated in the trajectory reference frame, defined by rotating the body from the straightened frame such that the center of mass velocity is in the forward direction. In the trajectory reference frame, gap is defined as the horizontal distance between the upstream and downstream segments and stagger as the vertical distance (figure 2C).

Beginning in the straightened frame, the center of mass position was removed to isolate the relative motion of the body about the center of mass. Next, the body was rotated about the lateral (\hat{X}) axis by the glide angle equation (5) such that the center of mass velocity was in the forward direction. The rotations of the body into the different frames are given by,

$$\vec{R}^S = \mathbf{C}^{I \rightarrow S} \cdot \vec{R}^I \quad (29)$$

$$\vec{R}^{S,c} = \vec{R}^S - \vec{R}_o^S \quad (30)$$

$$\vec{R}^F = \mathbf{C}^{S \rightarrow F} \cdot \vec{R}^{S,c} \quad (31)$$

where the superscripts denote the inertial (I), straightened (S), and trajectory reference (F) frames, and the rotation matrices are denoted by \mathbf{C} .

Once in the trajectory reference frame, we found intersections of the body spline with a vertical plane at the center of mass (figure 2D,E). The locations of the intersections defined where the gap and stagger values were calculated. For each intersection, we took the relative displacement between the upstream and downstream airfoils as the gap and stagger, respectively. Sometimes, the body intersected the vertical plane multiple times. During these instances, we defined two separate gap and stagger values from the first and second intersections and the second and third intersections.

Gap and stagger from previous kinematic measurements

Analysis of the center of mass trajectory revealed steep glides compared to previous kinematic measurements of snake glides (Socha et al., 2010; 2005). This observation prompted us to revisit data from these other studies to extract gap and stagger information. For this analysis, we used data from Socha et al. (2010), which was the previous best kinematics data. This previous experiment recorded late-phase gliding in two individuals, with four trials per

snake analyzed, of glides originating from a height of 15 m. The data comprise trajectories of five landmark points (head, 1/4 SVL, 1/2 SVL, 3/4 SVL, and vent), rotated into the trajectory reference frame. Gap and stagger values were estimated from these data as described above, using marker pairs — head-1/2, 1/4-3/4, and 1/2-vent — at time points when the lateral displacement of the marker pairs were the same. Time points with the same lateral displacement are an approximation to intersections of the body with the vertical plane passing through the center of mass; this approximation was made because the center of mass is not precisely known from the five-point data.

Assumptions

The analysis presented in this study is based on several layers of assumptions, beginning with the measured infrared marker trajectories. From the marker trajectories, the spline curve was used to represent the body as it moves through space. Next, the mass and width distributions were overlaid on the spline; the mass distribution was measured from anatomical snake sectioning, and the width distribution from photographs (Yeaton et al., 2020). The gap and stagger calculations are based on the spline, while the relative angle-of-attack and sweep angles of the wing segments both incorporate assumptions discussed below.

A necessary assumption for the quasi-steady force calculations is the orientation of the airfoil coordinate system. The airfoil coordinate system directly affects the aerodynamic force calculations, because it is one of two components that determine the angle of attack (the other being the average forward velocity vector of the snake along its trajectory). The need for an assumption arises from the fact that our kinematics data are limited: the IR system is assumed to have identified the centroid of the marker on the snake, which is along the dorsal backbone. As such, we have no quantitative information about the lateral positions (i.e., the width) of the snake's body. As an analogy, this situation is akin to identifying the root and tip of a bird's wing during flight, but not knowing the location of the leading and trailing edges. Without that information, it is impossible to specify the local angle of attack on any part of the snake's body. We selected a method to calculate the airfoil coordinate system that resulted in a reconstructed wing-body that was qualitatively similar to images of the snakes while airborne (figure 3G,H). The similarity included the twisting of the body at the 'U'-bends, the overall orientation of the straight segments, and the calculated forces varying continuously along the body. Because we lack the full kinematic data, we have no way of calculating the error in angle of attack in our model, but the visual similarity of model to imagery of the real gliding snake provides some small degree of confidence that the model can be informative and provide a basis to build upon.

The other aerodynamic assumptions are (1) extrapolation of lift and drag coefficients between angles of attack of 60° - 90° , (2) the use of simple sweep theory to account for the non-perpendicular body segments, and (3) quasi-steady aerodynamics. The lift extrapolation is based on the fact that the snake's cross-sectional shape is left-right symmetrical, and this shape at 90° will produce zero lift. The drag extrapolation was based on similarity of the shape to other triangular shapes, with experimental coefficients reported to be around 2 (Hoerner, 1965). The simple sweep theory assumption enabled the use of our current best understanding of flying snake aerodynamics, as no data exists on the relative orientation of the airflow to the body. Likewise, the quasi-steady

aerodynamics theory had not been tested on flying snake locomotion given our previously poorer understanding of the whole body motion during a glide. Overall, the data presented in this study should help guide future work to address the assumptions used here.

RESULTS AND DISCUSSION

Center of mass motion

The center of mass trajectory from the side and overhead views is shown in figure 4A,B for 43 trials from seven individuals. For the center of mass analysis, multiple glides from three individuals are shown separately, chosen because these individuals gave the greatest number of usable trials to analyze, and happened to span the observed mass range of animals tested. The side views indicate relatively steep glides compared to previous studies. The largest animal (snake 81, mass: 107.2 g) only covered about 4 m horizontally from an 8.3 m jump height. The lightest animal (snake 95, mass: 37.3 g) has more variation in the horizontal glide distance, but generally performed better and covered horizontal distances up to 5 m. Trial 618 (figure 4Aiii,Biii) was the best performing glide, as it shallowed fastest and covered the most horizontal distance. However, the snake landed on the target tree placed in the glide arena (figure 1A), so the maximum potential horizontal distance was not recorded; it is estimated that this snake could have glided 7 m horizontally. The overhead view of the center of mass trajectories (figure 4B) shows that the glide paths were generally not straight. The center of mass motion has broad arcs, but no discernible turning events were observed. The overhead view shows no oscillations of the center of mass due to undulation.

The dimensional velocity polar diagrams (figure 4C) indicate initial forward velocities at or below 2 m/s for all snakes. The velocity trajectories initially move vertically downwards on the diagram as the snakes accelerate downwards while keeping the horizontal velocity constant during the ballistic phase. The glide angle during this phase increases from roughly 0° to 60° – 75° before the velocity trajectory arcs upward. The shape of the arc upwards is similar across all glides and is consistent with motion onto the “terminal velocity manifold” in theoretical models of gliding (Yeaton et al., 2017; Nave Jr and Ross, 2019). For the smallest snake (figure 4Ciii), the trajectories curve upwards the most, indicating it progresses farthest through the glide. The curve upwards is more apparent when viewing the non-dimensional and rescaled velocity polar diagrams (figure 4D), as all effects of animal size have been removed. The glides that performed best, trial 618 from snake 95 and trial 505 from snake 88, progressed farthest on the velocity polar diagram and had higher initial horizontal velocities. The higher velocity likely caused the glide to transition more quickly, while slower horizontal velocities took longer to transition.

Lift and drag forces

The quasi-steady forces and center of mass accelerations are shown in figure 5 for the three individuals with the greatest number of usable glides. If quasi-steady theory properly accounts for the aerodynamic forces, the left and right plots in figure 5 should be the same. We see the same trends across individuals in regards to the forces and accelerations, but quasi-steady theory is insufficient to explain the aerodynamic forces on the snake. In general, the force estimates are smoother than the accelerations, with smaller

standard deviations during the trajectory. The lower standard deviation is due to only needing to perform one numerical derivative to calculate velocities, while the center of mass acceleration requires two derivatives, as well as integrating the forces having a filtering effect.

Both the average lateral force and lateral accelerations are near zero, indicating fairly good agreement between the accelerations and quasi-steady theory (figure 5A). The deviations are larger about the forward and vertical directions. The forward forces, which are the aerodynamic forces responsible for horizontal motion over the ground, are too low compared to the accelerations. The average accelerations peak at approximately 0.5 body weight (BW), while the forces peak at approximately 0.25 BW (figure 5B). In contrast, the vertical forces are higher than the accelerations. The vertical forces are responsible for offsetting the animal’s weight against gravity. The force time series indicate that more vertical force is produced than needed to support the weight (forces are above the dashed line in figure 5C). The accelerations are lower and only cross the supporting body weight threshold for the lightest snake. Therefore, the quasi-steady force estimates show qualitatively the same trends as the accelerations, but the forces are underestimated in the forward direction and overestimated in the vertical direction.

Across individuals, the accelerations about the lateral direction are similar. However, there is a qualitative difference in the forward and vertical directions between the lightest and heaviest individuals (snake 95, mass: 37.3 g and snake 81, mass: 107.2 g) with a difference in mass of approximately $2.9\times$. The forward acceleration of the lighter snake peaks and then decreases near the end of the glide, whereas the heavier snake does not show this behavior. The vertical accelerations show the lighter snake accelerating upward near the end of the trajectory, whereas the heavier snake does not. The medium-heavy snake (snake 91, mass: 71 g, mass ratio of $1.9\times$ compared to the lighter snake) appears to be accelerating slightly upwards (figure 5C).

Aerodynamic force errors and adjustments

The absolute force errors, defined as the absolute difference between the calculated center of mass acceleration and the resultant aerodynamic force, are shown in figure 6A for all of the seven snakes analyzed. Errors are near zero about the lateral direction. The forward force error is approximately 0.25 BW, while the vertical force error is approximately -0.5 BW. The physical interpretation of these errors is that that quasi-steady theory overestimates drag and underestimates lift, as the drag force acts predominantly in the vertical direction, while the lift force acts predominantly in the forward direction. Decreasing drag and increasing lift will rotate the resultant aerodynamic force vector forward and reduce the error.

The required multipliers to the lift and drag forces to reduce the total error to zero are shown in figure 6B. The lift force needs to be multiplied by $1.35\times$ and the drag force needs to be multiplied by $0.6\times$ of the quasi-steady values. Note that the change in drag is approximately constant throughout the glide, while the change in lift decreases from approximately $2\times$ to $1\times$ as the glide progresses. The force multipliers thus indicate that quasi-steady theory consistently overestimates the total drag force by approximately 40% and underestimates the total lift force by approximately 35%.

Lift and drag distributions

The time-varying lift and drag distributions for the best performing glides are shown in figure 7 for different heights as the animals glide. The force distributions have the same orientation as predicted by quasi-steady theory, but have been scaled using the lift and drag multipliers such that the total force errors are near zero. Therefore, the true local lift and drag force may be quite different than shown. By 10% through the glide ($z/h_0 = 0.9$, the first row in figure 7), the snake bodies have already formed the ‘S’-shaped glide posture, and lift and drag forces are being produced. As the glides progress, the smaller animal (snake 95, mass: 37.3 g, SVL: 64.4 cm) forms a tight body posture, with the posterior body dropping below the head. The larger animal (snake 88, mass: 71.9 g, SVL: 88.8 cm) has a more open body posture, with fewer spatial periods of bending, and a more horizontal orientation.

There are commonalities in the force distributions for both animals. The drag force is continuous along the body, including along the straight segments and along the ‘U’-bends. In contrast, consistent with the simple sweep theory assumption, the lift force decreases to zero at the ‘U’-bends, and is largest along the straight segments. The transition region to zero lift is small and does not extend over the entire ‘U’-bend region. The small transition region is likely related to low sweep angles before and after the ‘U’-bends (figure 8E,F). The estimated force produced by the tail is small because of its small width. This small width also results in lower Reynolds numbers (figure 8A,B). For snake 88, the body is initially highly swept, with the straight segments angled roughly 45° relative to the forward direction. However, the model still indicates that these areas produce appreciable lift force. The side views of the glides indicate that the drag force acts in the vertical direction and against the direction of forward motion. The lift force is angled upwards relative to the horizontal and along the direction of forward motion.

For the glides shown in figure 7, the time histories of the Reynolds numbers, angles of attack, sweep angles, and dynamic pressure fraction distributions are shown in figure 8. The Reynolds number (figure 8A,B) broadly tends to increase throughout the glide because the snake’s airspeed increases as it accelerates. The larger animal has higher Reynolds numbers due to its greater width and speed. The Reynolds numbers peak midway along the body, where the animal is widest. The angles of attack are high, ranging from 60° to 90° at various points along the body. The ‘U’-bends have the highest angles of attack (shown as dashed lines in figure 8A,B), which results in the locations of zero lift production in figure 7. The ‘U’-bends have the highest sweep angles, and locations along the body near the ‘U’-bends have low sweep values. Even along the straight segments, the sweep angle is generally greater than 30° . Lastly, the dynamic pressure fraction is shown in figure 8G,H, with the 75% contour highlighted. Values of 100% indicate no decrease in lift or drag due to the swept wing, whereas values of 0% indicates no force being produced because of sweep. The straight segments of the snake maintain the most dynamic pressure, although there are regions where this is not the case (figure 8G and figure 7 for snake 95 at 0.7 and 0.6 of the height fallen).

Gap and stagger

The relative spacing of the perpendicular body segments for all glides and at different progressions through the glide are shown in figure 9A and summarized in table 1. Initially, the distributions of

gap (horizontal spacing) and stagger (vertical spacing) show high spread, which decreases later in the glide. During the first quarter of the glides, the median gap is 3.0 c (chord) and the median stagger is 3.7 c. The second quarter of the glides exhibits the same median stagger of 3.7 c, but the median gap decreases to 1.0 c. During the third and fourth quarters of the glides, the median gap is effectively 0 c, while the median stagger is 4.2 c. As a measure of distribution spread, we use the interquartile range (IQR). Initially, the gap and stagger interquartile range is (3.8 c, 2.4 c), which decreases to (2.7 c, 1.8 c) during the second quarter of the glide. The interquartile ranges decrease further to (2.1 c, 1.7 c) and (2.0 c, 1.3 c) during the second half of the glides. The gap and stagger distributions indicate gaps that are near zero and even negative. A gap of zero indicates the forward airflow contacts the anterior and posterior body simultaneously, while a negative gap indicates the rear airfoil leads the front airfoil. Staggers are generally positive, indicating that the rear airfoil is below the front airfoil relative to the airflow.

Overlaid on the joint distributions are the gap and stagger measurement locations for wake interaction effects (Jafari et al., 2021). Gap and stagger combinations are observed in the aerodynamic interaction region, although these combinations are relatively rare. Wake interaction effects are most prominent along the top row, with the rear airfoil directly behind the front airfoil. There are also wake interaction effects along the second row, but the effect is smaller. The gap and stagger measurement locations initially overlap with the observed gap and stagger distributions, but the overlap is less later in the glide, as the observed distribution moves to a gap of zero.

The angles of attack of the front and rear airfoils are shown in figure 9B. The angle of attack of the rear airfoil is correlated with the angle of attack of the front airfoil. Initially, angles of attacks are very high, upwards of 70° to 90° , with the median angle of attack being 74° for both the front and rear airfoils. As the glides progress, the spread of the angle of attack distribution decreases, and the median angle of attack ultimately decreases to 56° for the front airfoil and 65° for the rear airfoil. All angles of attack were high, indicating large drag coefficients and small lift coefficients (figure 2A). The sweep angles of the front and rear airfoils (figure 9C) do not follow a clear trend as do the angle of attacks. Initially, there is a large cluster of high sweep angles, which may be due to the jump and body formation phase of the glide. Later in the glide, the higher sweep angles are not seen, but there is no clear trend relating the sweep angle of the front and rear airfoils.

Lastly, gaps and staggers from this study and estimated gaps and staggers from a previous study with only five markers on the snake (Socha et al., 2010) are shown in figure 9D. The gaps from the five marker trials are much greater than observed in this study. The steep glides from this study have a gap of approximately 0 c, while the shallow glides from the previous study have a gap greater than 5 c, although the staggers are similar. The gap and stagger combinations from the five-point trials are generally in the wake interaction region, although few time points from the current study are located in the wake interaction region. The third panel of figure 9D indicates that although uncommon, gap and stagger configurations in the wake interaction region are observed in the present study.

Center of mass motion

This study of flying snake glide trajectories provides the first measurements of the snake's center of mass informed by the whole body. The overhead and side views of the glide trajectory provide our first measurements of the center of mass motion of flying snake glides. The recorded glides were steeper than would be anticipated from previous studies, with a horizontal glide distance of only 4 m from a jump height of 8.3 m, whereas maximum glides from a previous experiment averaged 10.1 m horizontally from a jump height of 9.6 m (Socha et al., 2005). There are several possible explanations for this difference, including the more massive snakes used in the present study, physical markers being placed on the body, lack of visual cues from the indoor glide arena, potential colony effects, or because wild-caught snakes are more accustomed to gliding. Alternatively or additionally, only the best performing glides from previous studies were analyzed in detail, whereas all trials, regardless of performance, were analyzed in the present study. The larger mass directly affects the wing loading of the animal, with predictable results in the velocity polar diagram; see figure 4. To address visual cues, a target tree was placed in the arena (see figure 1), as has been done for previous studies. There was no discernible difference when handling the animals and encouraging them to jump. Additionally, the physical tape markers, as opposed to painted markers, were placed carefully on the animal's dorsal surface to minimize disturbance to their flattening. As a control, one snake was left unmarked and did not show noticeably different glide behavior or performance than the marked snakes. Although the glides were steep, the increased spatial and temporal resolution enabled us to fully quantify the position of the body in much greater detail than in previous studies. This improved understanding enables us to calculate the center of mass, as well as estimate aerodynamic forces, and measure the gap and stagger of different body segments.

The overhead view of the glide path (figure 4B) did not show obvious center of mass deviations related to undulation. These data show the unfiltered center of mass, so the smoothing effects of digital filtering are not present. We do see broad arcing turns, although no distinct turning events were observed during the trials. This arcing motion could be due to the initial jump conditions and a result of stabilizing the rotational motion (Yeaton et al., 2020). There is one trajectory that followed a fairly straight course, trial 413 from snake 91 (figure 4Bii), from the launch branch to the target tree. We recorded only a few glides that landed on the tree.

The velocity polar diagrams (figure 4C,D) have been discussed previously from a theoretical modeling perspective; see (Yeaton et al., 2017; Nave Jr and Ross, 2019). The empirical velocity polar diagrams provided here support several theoretical predictions from those previous studies. First, the wing loading rescaling enables comparisons between individuals that vary in mass. The theoretical studies predicted that smaller individuals would progress further through the diagram during a glide and show better glide performance, which was seen in this study with individuals varying by a factor of three in mass. Additionally, a greater initial forward velocity was predicted to more quickly reach a steady state glide and perform better. Here, we found the best performing glides did indeed have greater initial forward velocities. All diagrams show a characteristic turn that signifies the transition from the ballistic to the shallowing phases of gliding. The theoretical model predicted that a trajectory in the velocity polar diagram, starting from a horizontal jump, will accelerate quickly downwards

before curving upwards, transitioning onto the terminal velocity manifold, a higher-dimensional analogue to the terminal velocity speed. This transition point occurs for different absolute airspeeds for different individuals. However, the rescaled diagrams show that the transition occurs for a non-dimensional speed of approximately one, which is approximately the terminal velocity speed.

Potential reasons for discrepancy

Quasi-steady theory was insufficient to explain the aerodynamic forces produced during short glides in flying snakes. When compared to the experimentally determined center of mass acceleration, the predicted quasi-steady lift forces were 35% lower and the quasi-steady drag forces were 40% higher. We found that the difference in drag was constant throughout the glides, whereas the difference in lift decreased throughout the glide; see figure 6.

One possibility for the lift multiplier changing with progress through the glide is that initially the angles of attack along the wing-body are high. As the glide progresses, the angles of attack decrease from 70° – 90° at the start to 50° – 70° at the end of the glide. The lift and drag curves are substantially different at high angles of attack; the lift coefficient is near zero, while the drag coefficient is at a maximum; see figure 3A. The relative change in the lift and drag coefficients also varies as the angle of attack is decreased. From 90° to 60° , the extrapolated lift coefficient increases from 0 to about 1, while the extrapolated drag coefficient only decreases from approximately 2 to 1.6. Therefore, the modification to the lift force is more sensitive during the initial portion of the glide as the angle of attack decreases from a high value. While the lift and drag extrapolated values at $\alpha = 90^\circ$ are based on theory for geometrically similar airfoils (Yeaton et al., 2020), the true lift and drag values in this regime of angle of attack are unknown, as previous experiments only measured up to 60° . The most likely difference in lift or drag coefficients in this regime are likely to be in drag, because the estimate at 90° is less certain than in lift (which is zero at 90° due to the symmetry of the airfoil with respect to the airflow at this configuration). However, the results of this study show that the quasi-steady model overestimates drag, suggesting that our extrapolation was not the major factor in the difference. More generally, it is likely that the discrepancy between model and reality stems from the nature of the kinematic data: in the trials analyzed here, the snake was not only undulating but continuously accelerating throughout the trajectory, yet the model takes a quasi-static approach, which intrinsically does not include acceleration. It would be interesting to apply the model in future studies to non-accelerating parts of a glide, which could in theory be obtained from snakes launched from a greater height. Such work would build on recent theoretical advances of our understanding of gliding across all animals including flapping flyers (Cheney et al., 2020; Usherwood et al., 2020; KleinHeerenbrink et al., 2022), beyond the gliding-restricted taxa like flying snakes.

Tandem airfoil effect: Gap, stagger, and airflow orientation

Tandem airfoil effects, due to wake interactions between a leading airfoil and a trailing airfoil, are an unsteady aerodynamic effect. They were considered here as a potential reason for the insufficiency of quasi-steady theory. The distributions of gap and stagger, and how they change depending on progress through the glide (figure 9A), revealed zero or even negative gap values at the end of the glide. The gap and stagger results indicate that flying snakes

use a wide range of body configurations relative to the airflow. Notably, during all glides, the gap and stagger values spend little time in the region where wake interaction effects are greatest (figure 9D), from which it can be concluded that this effect is not the reason for the insufficiency of quasi-steady theory.

While the configurations may not be advantageous from an aerodynamics and glide performance perspective, they may serve ecologically relevant functions. For example, snakes executing short glides, or falling near vertically, may do so to escape predators. Falling straight downwards still requires controlling aerodynamic and inertial forces to ensure stability, but will not result in substantial horizontal travel. Steep glides may allow the snakes to fall away from the predator while staying on the same tree, or in the nearby area.

Flying snakes therefore have a large performance envelope within which to operate. Some glides can be viewed as predominantly falling, in which the animal moves vertically downward or only covers a few meters horizontally, whereas other glides cover significant horizontal distance, possibly to escape to a different tree. It is known that other gliding animals (Khandelwal et al., 2023), such as flying squirrels and *Draco* lizards, have higher shallowing rates and shallower glides than flying snakes (Socha et al., 2015), but they may not be able to execute very steep glides. The morphing wing-body of flying snakes may be particularly well suited to stabilize short glides, as it possibly allows the animal to correct for rotational torques. Additionally, the multi-wing configuration may enable wake interactions that increase glide performance (figure 9D), although this may not be volitional and may simply be an artifact of the shallowing glide.

Future work

Future studies are needed to address the assumptions used in this work. The biggest kinematic assumption is the airfoil coordinate system that is overlaid on the spline fit of the body. This assumption was used because the orientation of the body was not resolvable from the marker time series. The airfoil coordinate system directly affects the force estimates, as well as angle of attack and sweep angle estimates. Future experiments, with greater camera coverage, may be able to measure body orientation with higher resolution.

The next assumptions to be addressed are quasi-steady theory and simple sweep theory. Both assumptions were applied so that previously measured lift and drag coefficients could be used. An alternative to using quasi-steady force coefficients and simple sweep theory would be to perform anatomically accurate computational fluid dynamics (CFD) simulations, with a moving mesh derived from the kinematics analysis. This analysis would account for unsteady fluid phenomena, and provide details about wake interaction, vortex shedding, and flow at the ‘U’-bends of the snake. This analysis would also provide insights into span-wise flow along the straight body segments. In fact, a full-body CFD analysis has been conducted recently, but it treated the snake in an idealized fashion, with the motion of the body sinusoidal, confined to a single, horizontal plane, in a non-accelerating regime (Gong et al., 2022). This CFD study provides new insight into potential aerodynamic mechanisms including enhancement by leading and trailing edge vortices, and it would be useful to conduct a similar force comparison with experimental data as done here. As an alternative to computational models, physical or robotic models could be tested in air or water tunnels, as in (Holden et al., 2014), or in a

tow tank, in which the model could be accelerated. Flow and force measurements can then be taken of the whole snake model, or of straight segments at different attack and sweep angle combinations (figure 8C,D). Finally, it would be informative to compare model results with trajectories that include shallower gliding seen in prior studies (Socha, 2002; Socha et al., 2005; Socha and LaBarbera, 2005; Socha et al., 2010).

In some ways, the reciprocal progression of experiment and model development suggested by this study parallels the early history of flight studies of birds, bats, and insects (Alexander, 2003; Biewener and Patek, 2018; Dudley, 2000). Each of these groups shared common features of locomotion, but more detailed understanding of kinematics and aerodynamics was required to refine the theoretical understanding of their flight. In a parallel way, this study similarly represents a foundational step forward in understanding how flying snakes glide, providing new inspiration for future work.

CONCLUSION

Using a new kinematics analysis of the center of mass trajectory and body orientation, we tested if quasi-steady theory can predict the time-varying lift and drag forces on flying snakes. Quasi-steady theory was insufficient to fully explain the forces acting on the body. Our results indicate that unsteady and 3D aerodynamic effects are likely important for snake flight, even during short glides. During some glides, we did find body configurations where the anterior body was located where unsteady wake interaction effects are possible, but this is unlikely to explain the shortcomings of the applied quasi-steady theory. However, wake interaction effects may be more prominent during late phase gliding. The time-varying body posture and orientation can be used in future computational dynamics and physical modeling studies to elucidate unsteady and 3D aerodynamic phenomena during snake flight.

Acknowledgements

We thank the Virginia Tech Institute for Creativity, Arts, and Technology (ICAT) for facilities access, crew support, and funding. In particular, we thank Tanner Upthegrove, Nate McGowan, and Benjamin Knapp. We thank Gary Nave, Talia Weiss, Michelle Graham, Jack Whitehead, Joel Garrett, and Grant Baumgardner for assisting with the kinematics experiments. We thank Hodjat Pendar for help with developing the mathematical model of snake flight. We thank Barry Robert, Julie Settlage, and Amy Rizzo for help with IACUC.

Competing interests

The authors declare no competing or financial interests.

Contribution

JJS and IJY conceived the project, IJY and JJS designed and conducted the experiments; IJY and SDR developed the mathematical model; IJY analyzed the experimental data, implemented the simulations, and analyzed the simulation output; IJY, SDR, and JJS wrote the manuscript.

Funding

This work was supported by the National Science Foundation under grant 1351322 to JJS, grants 1537349 and 1922516 to SDR, and grants 0966125 and 2027523 to SDR and JJS. IY was supported by the Biological Transport (BIOTRANS) Interdisciplinary Graduate Education Program at Virginia Tech.

Data availability

Data from the glide trials are available at <https://github.com/TheSochaLab/Undulation-enables-gliding-in-flying-snakes>. Code used to analyze the glide trials and perform the glide simulations is available at <https://github.com/TheSochaLab/Quasi-steady-aerodynamic-theory-under-predicts-glide-performance-in-flying-snakes>.

REFERENCES

- Alexander, R. M.** (2003). *Principles of Animal Locomotion*. Princeton: Princeton University Press, 371 pp.
- Bahlman, J. W., Swartz, S. M., Riskin, D. K. and Breuer, K. S.** (2013). Glide performance and aerodynamics of non-equilibrium glides in northern flying squirrels (*Glaucomys sabrinus*). *J R Soc Interface* **10**.
- Biewener, A. and Patek, S.** (2018). *Animal Locomotion*. Oxford University Press, 223 pp.
- Byrnes, G., Lim, N. T.-L. and Spence, A. J.** (2008). Take-off and landing kinetics of a free-ranging gliding mammal, the Malayan colugo (*Galeopterus variegatus*). *Proc R Soc B* **275**, 1007–1013.
- Cheney, J. A., Stevenson, J. P., Durston, N. E., Song, J., Usherwood, J. R., Bomphrey, R. J. and Windsor, S. P.** (2020). Bird wings act as a suspension system that rejects gusts. *Proceedings of the Royal Society B* **287**, 20201748.
- Chin, D. D. and Lentink, D.** (2016). Flapping wing aerodynamics: from insects to vertebrates. *J Exp Biol* **219**, 920–932.
- Dickinson, M. H., Lehmann, F.-O. and Sane, S. P.** (1999). Wing rotation and the aerodynamics basis of insect flight. *Science* **284**, 1954–1960.
- Dudley, R.** (2000). *The Biomechanics of Insect Flight*. Princeton: Princeton University Press, 476 pp.
- Dudley, R. and Ellington, C. P.** (1990). Mechanics of forward flight in bumblebees. II. Quasi-steady lift and power requirements. *J Exp Biol* **148**, 53–88.
- Ellington, C. P.** (1984). The aerodynamics of hovering insect flight. I. The quasi-steady analysis. *Phil Trans R Soc L. B* **305**.
- Ellington, C. P., van den Berg, C., Willmott, A. P. and Thomas, A. L. R.** (1996). Leading-edge vortices in insect flight. *Nature* **384**, 626–630.
- Gong, Y., Wang, J., Zhang, W., Socha, J. J. and Dong, H.** (2022). Computational analysis of vortex dynamics and aerodynamic performance in flying-snake-like gliding flight with horizontal undulation. *Physics of Fluids* **34**, 121907.
- Hedenström, A., Johansson, L. C., Wolf, M., Von Busse, R., Winter, Y. and Spedding, G. R.** (2007). Bat flight generates complex aerodynamic tracks. *Science* **316**, 894–897.
- Hoerner, S. F.** (1965). *Fluid-Dynamic Drag: Practical Information on Aerodynamic Drag and Hydrodynamic Resistance*. Hoerner Fluid Dynamic.
- Holden, D., Socha, J. J., Cardwell, N. D. and Vlachos, P. P.** (2014). Aerodynamics of the flying snake *Chrysopelea paradisi*: how a bluff body cross-sectional shape contributes to gliding performance. *J Exp Biol* **217**, 382–394.
- Jafari, F., Holden, D., LaFoy, R., Vlachos, P. P. and Socha, J. J.** (2021). The aerodynamics of flying snake airfoils in tandem configuration. *Journal of Experimental Biology* **224**.
- Khandelwal, P. C. and Hedrick, T. L.** (2022). Combined effects of body posture and three-dimensional wing shape enable efficient gliding in flying lizards. *Scientific Reports* **12**, 1–11.
- Khandelwal, P. C., Ross, S. D., Dong, H. and Socha, J. J.** (2023). *Convergence in Gliding Animals: Morphology, Behavior, and Mechanics*, pp. 391–429. Cham: Springer International Publishing.
- KleinHeerenbrink, M., France, L. A., Brighton, C. H. and Taylor, G. K.** (2022). Optimization of avian perching manoeuvres. *Nature* **607**, 91–96.
- Krishnan, A., Socha, J. J., Vlachos, P. P. and Barba, L. A.** (2014). Lift and wakes of flying snakes. *Phys Fluids* **26**, 031901.
- Maxworthy, T.** (1981). The fluid dynamics of insect flight. *Ann Rev Fluid Mech* **13**, 329–350.
- McCay, M. G.** (2001). Aerodynamic stability and maneuverability of the gliding frog *Polypedates demmysi*. *J Exp Biol* **204**, 2817–2826.
- McGuire, J. A.** (2003). Allometric prediction of locomotor performance: an example from southeast asian flying lizards. *Am Nat* **161**, 337–349.
- McGuire, J. A. and Dudley, R.** (2005). The cost of living large: comparative gliding performance in flying lizards (Agamidae: *Draco*). *Am Nat* **166**, 93–106.
- Miklasz, K., LaBarbera, M., Chen, X. and Socha, J. J.** (2010). Effects of body cross-sectional shape on flying snake aerodynamics. *Exp Mech* **50**, 1335–1348.
- Muijres, F. T., Johansson, L. C., Barfield, R., Wolf, M., Spedding, G. R. and Hedenstrom, A.** (2008). Leading-edge vortex improves lift in slow-flying bats. *Science* **319**, 1250–1253.
- Nave Jr, G. K. and Ross, S. D.** (2019). Global phase space structures in a model of passive descent. *Communications in Nonlinear Science and Numerical Simulation* **77**, 54–80.
- O’Dor, R., Stewart, J., Gilly, W., Payne, J., Borges, T. C. and Thys, T.** (2013). Squid rocket science: how squid launch into air. *Deep Sea Res Part II Top Stud Ocean*. **95**, 113–118.
- Park, H. and Choi, H.** (2010). Aerodynamic characteristics of flying fish in gliding flight. *J Exp Biol* **213**, 3269–3279.
- Socha, J. J.** (2002). Gliding flight in the paradise tree snake. *Nature* **418**, 603–604.
- Socha, J. J.** (2011). Gliding flight in *Chrysopelea*: turning a snake into a wing. *Integ Comp Biol* **51**, 969–982.
- Socha, J. J., Jafari, F., Munk, Y. and Byrnes, G.** (2015). How animals glide: from trajectory to morphology. *Can J Zool* **93**, 901–924.
- Socha, J. J. and LaBarbera, M.** (2005). Effects of size and behavior on aerial performance of two species of flying snakes (*Chrysopelea*). *J Exp Biol* **208**, 1835–1847.
- Socha, J. J., Miklasz, K., Jafari, F. and Vlachos, P. P.** (2010). Non-equilibrium trajectory dynamics and the kinematics of gliding in a flying snake. *Bioinspir Biomim* **5**, 045002.
- Socha, J. J., O’Dempsey, T. and LaBarbera, M.** (2005). A 3-D kinematic analysis of gliding in a flying snake, *Chrysopelea paradisi*. *J Exp Biol* **208**, 1817–1833.
- Usherwood, J. R., Cheney, J. A., Song, J., Windsor, S. P., Stevenson, J. P., Dierksheide, U., Nila, A. and Bomphrey, R. J.** (2020). High aerodynamic lift from the tail reduces drag in gliding raptors. *Journal of Experimental Biology* **223**, jeb214809.
- Videler, J. J., Stamhuis, E. J. and Povel, G. D. E.** (2004). Leading-edge vortex lifts swifts. *Science* **306**, 1960–1962.
- Warrick, D. R., Tobalske, B. W. and Powers, D. R.** (2005). Aerodynamics of the hovering hummingbird. *Nature* **435**, 1094–1097.
- Winter, D. A.** (2009). *Biomechanics and Motor Control of Human Movement*. John Wiley & Sons.
- Yeaton, I. J., Ross, S. D., Baumgardner, G. A. and Socha, J. J.** (2020). Undulation enables gliding in flying snakes. *Nature Physics* .
- Yeaton, I. J., Socha, J. J. and Ross, S. D.** (2017). Global dynamics of non-equilibrium gliding in animals. *Bioinspir Biomim* **12**, 026013.

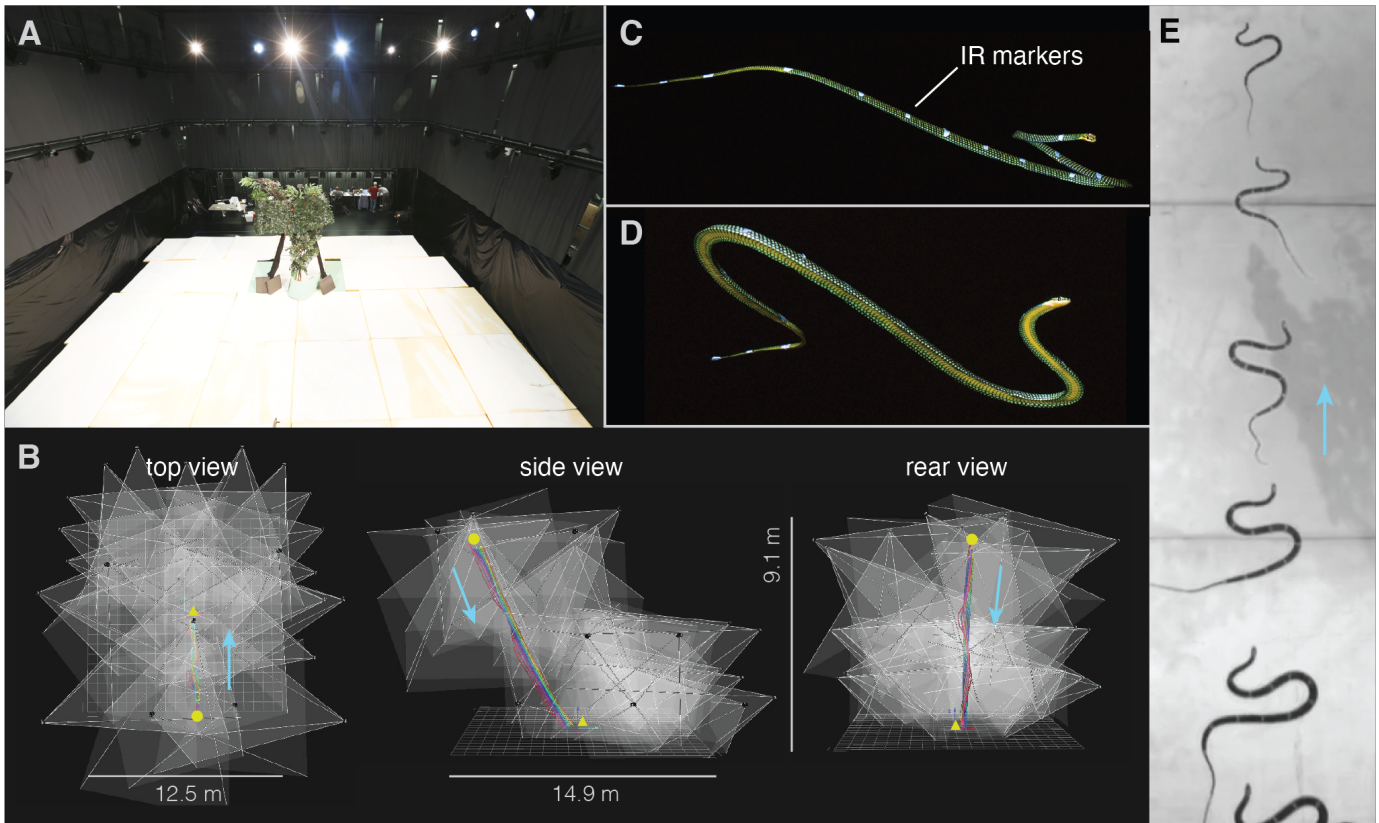


Fig. 1. Indoor glide arena and glide trial experiments. (A) View inside "The Cube", a black-box theatre equipped with launch platform, high-speed motion capture cameras, and target tree. The floor was covered with large foam pads. (B) Top, side and rear views of the motion capture camera coverage cones. The IR marker trajectories for one trial are shown, with the jump and landing locations indicated by the yellow markers. (C,D) *C. paradisi* in an 'S'-shaped glide posture. The infrared tape markers can be seen along the dorsal surface of the snake in C, and around the tail in D. (E) Select snapshots of a snake in its aerial trajectory from an overhead high-speed camera, stitched together using Photoshop. Reproduced with permission from (Yeaton et al., 2020)

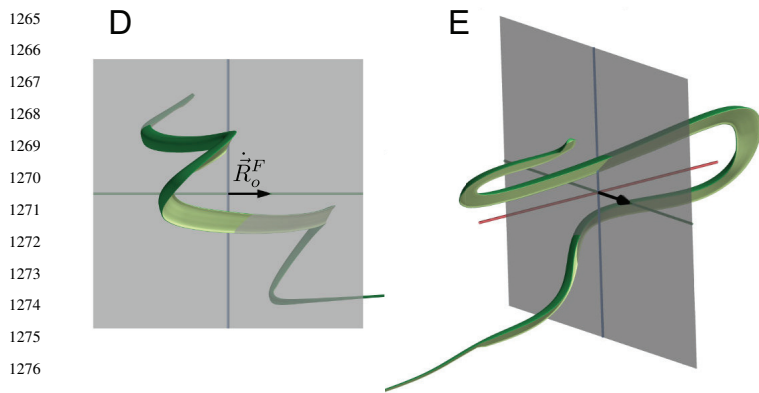
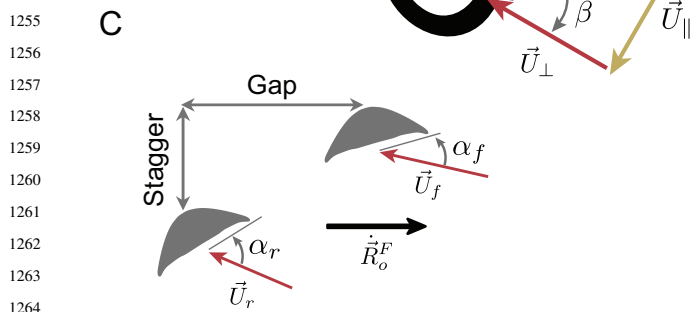
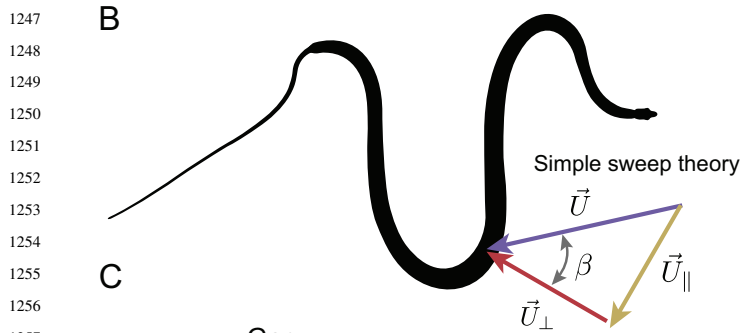
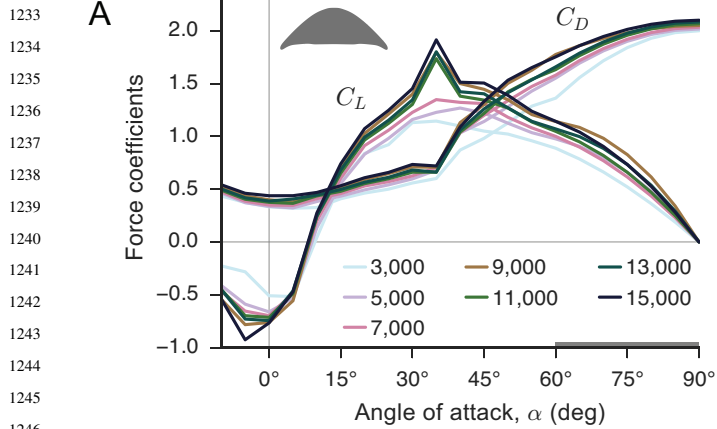
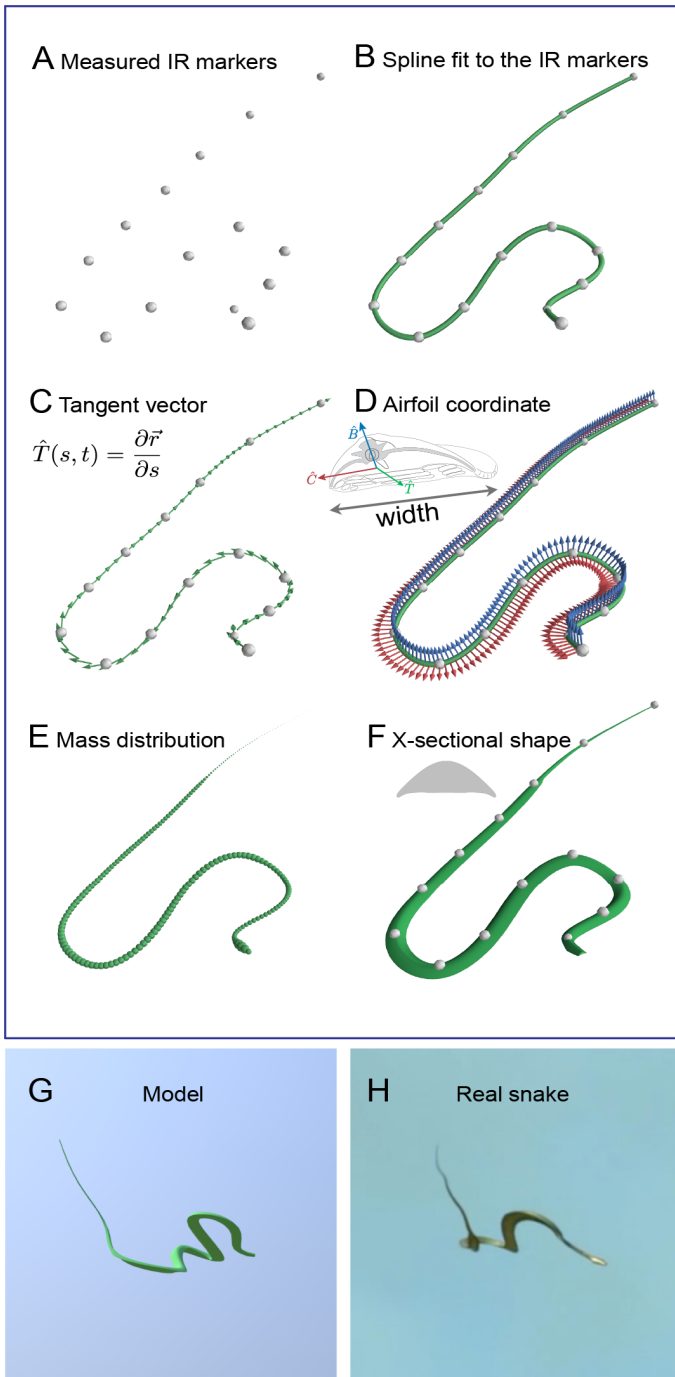


Fig. 2. Quasi-steady aerodynamics and gap and stagger calculations. (A) Quasi-steady lift and drag coefficients for different angles of attack and Reynolds number, using values from (Holden et al., 2014). The coefficients for $\alpha > 60^\circ$ are polynomial extrapolations such that the lift and drag coefficients match a triangular bluff body at $\alpha = 90^\circ$ (Hoerner, 1965; Yeaton et al., 2017). (B) Simple sweep theory and sweep angle calculation. The perpendicular velocity component is used in the force calculations, and is found by removing the velocity component parallel to the local tangent direction. (C) Definition of gap, stagger, and angle of attack of the snake in the trajectory reference frame. Gap is the horizontal spacing and stagger is the vertical spacing. Both the front and rear airfoils have different angles of attack, sweep angles, and different local velocities. (D,E) Two time instances from a glide showing intersections of the body with the plane through the center of mass. The locations of these intersections are used to calculate gap and stagger. The body is rotated to the trajectory reference frame, with the center of mass velocity in the $+y$ -direction, denoted by the black arrow. The time point in (D) is from 53% through the glide, while (E) is from 90%. The dorsal surface is indicated in green and the ventral surface in yellow.

1289
1290
1291
1292
1293
1294
1295
1296
1297
1298
1299
1300
1301
1302
1303
1304
1305
1306
1307
1308
1309
1310
1311
1312
1313
1314
1315
1316
1317
1318
1319
1320
1321
1322
1323
1324
1325
1326
1327
1328
1329
1330
1331
1332
1333
1334
1335
1336
1337
1338
1339
1340
1341
1342
1343
1344

1345
1346
1347
1348
1349
1350
1351
1352
1353
1354
1355
1356
1357
1358
1359
1360
1361
1362
1363
1364
1365
1366
1367
1368
1369
1370
1371
1372
1373
1374
1375
1376
1377
1378
1379
1380
1381
1382
1383
1384
1385
1386
1387
1388
1389
1390
1391
1392
1393
1394
1395
1396
1397
1398
1399
1400



1401
1402
1403
1404
1405
1406
1407
1408
1409
1410
1411
1412
1413
1414
1415
1416
1417
1418
1419
1420
1421
1422
1423
1424
1425
1426
1427
1428
1429
1430
1431
1432
1433
1434
1435
1436
1437
1438
1439
1440
1441
1442
1443
1444
1445
1446
1447
1448
1449
1450
1451
1452
1453
1454
1455
1456

Fig. 3. Method of reconstructing the morphing wing-body of flying snakes from recorded infrared marker (IR) trajectories. Each image shows the reconstruction step from one trial at the same time instance. (A) The measured IR markers provide a discrete representation of the body. (B) Cubic splines are fit to the IR markers, providing a continuous representation. (C) The tangent vector, \hat{T} , is used, along with the vertical direction, to define the airfoil coordinate system in (D). The width of the body is taken to define the chord-line, \hat{C} , and \hat{B} points upward through the backbone. (E) Mass distribution overlaid on the spline, visualized as spherical markers with radius proportional to the mass. The head and mid-body are relatively more massive; the tail only accounts for $\approx 9\%$ of the snake's mass. (F) Complete reconstruction of the morphing wing-body, showing the *C. paradisi* cross section overlaid on the spline, incorporating the orientation from (D) and the width distribution. (G) and (H) compare the output of this reconstruction with an image of a real snake, both in side view of a snake in a glide trajectory. (G) is from snake 95 in this study; the full model can be viewed here. (H) is from a different *C. paradisi* specimen from a previous filming session (courtesy of National Geographic Television).

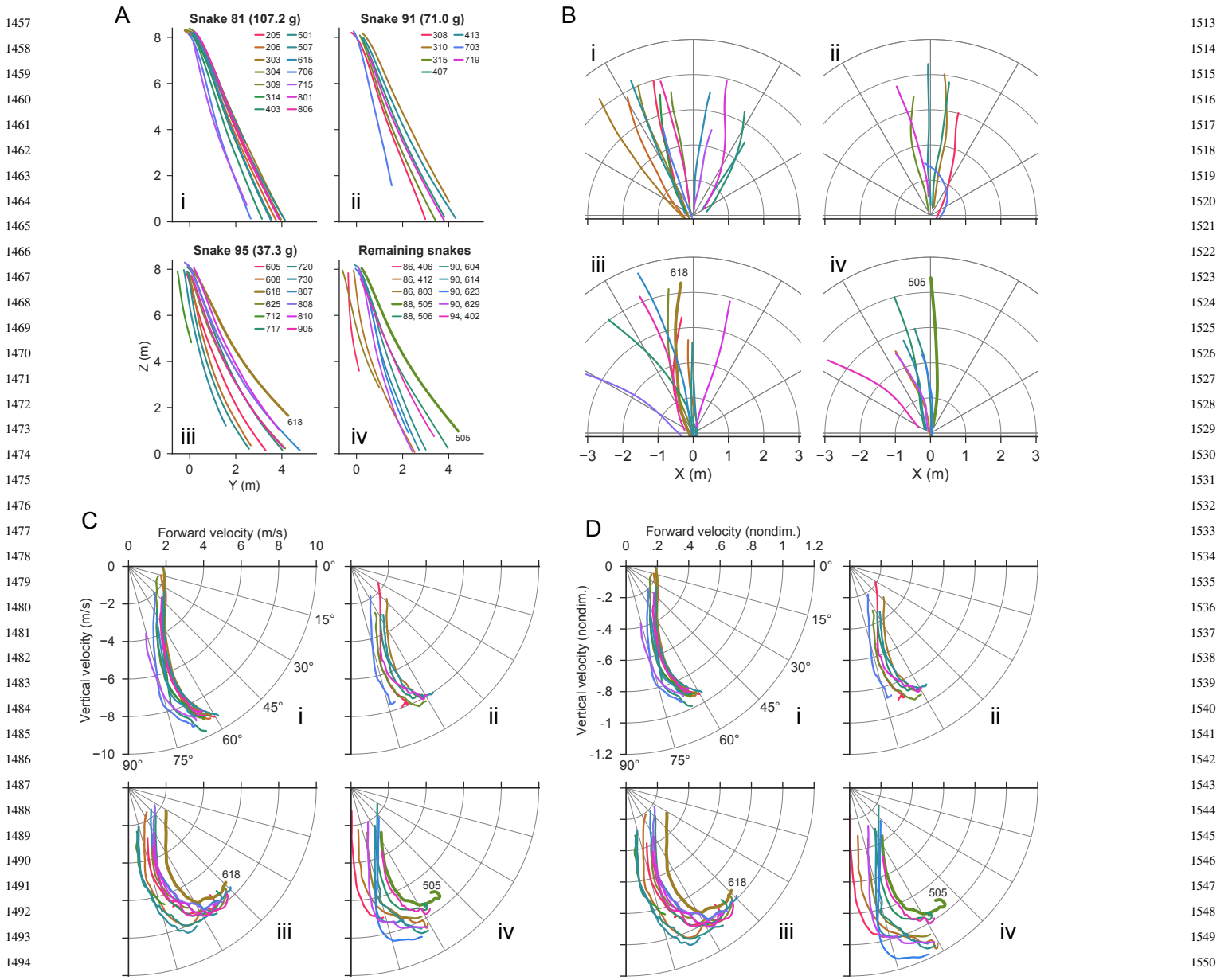
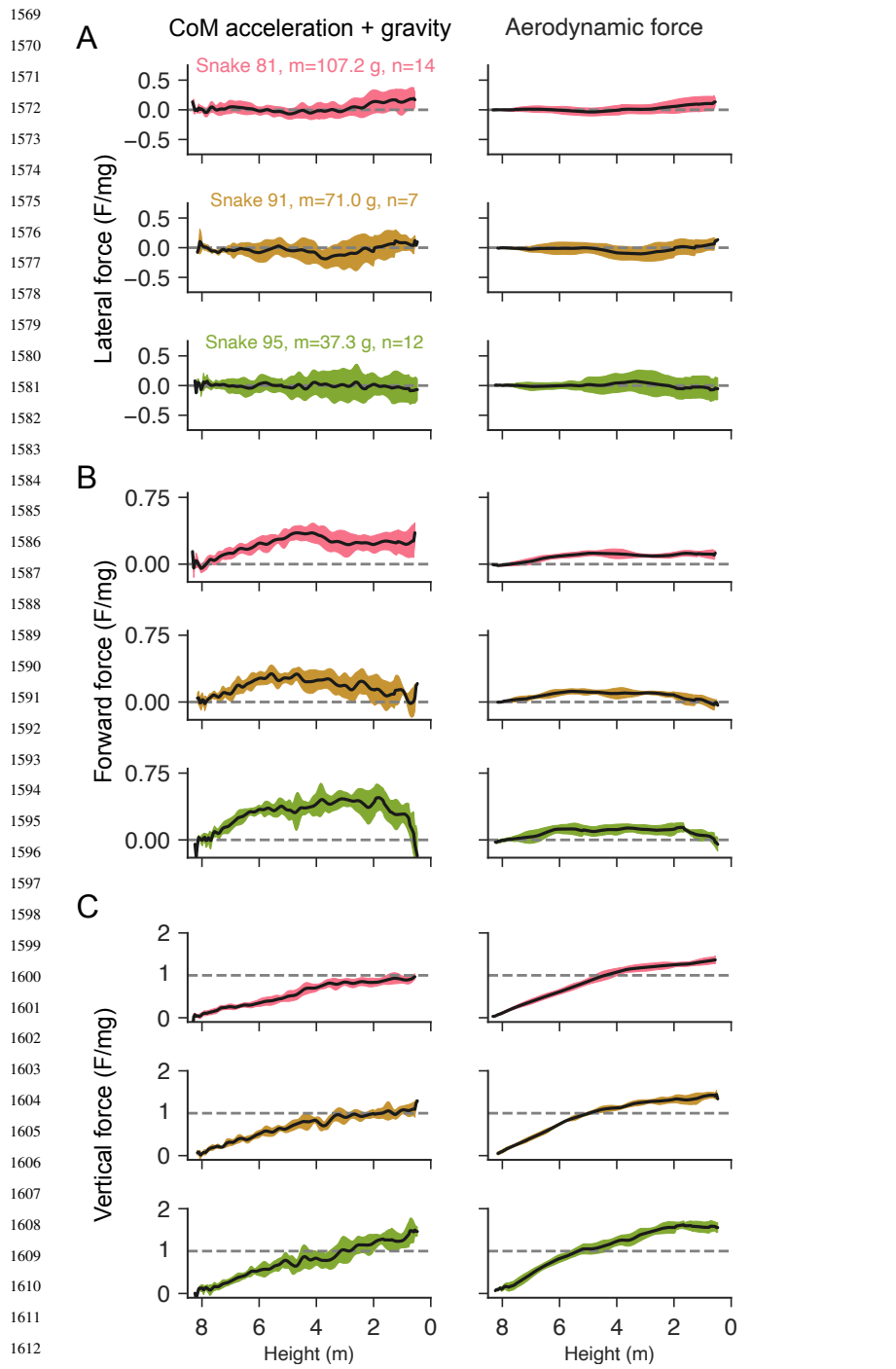


Fig. 4. Overview of trajectory dynamics for 43 trials from seven flying snakes. (A) Side view of the glide path in the straightened frame. Three of the panels are for three individuals that gave the greatest number of usable glides and spanned the entire mass range of snakes used. The last panel shows glides for four additional individuals. Different trials for each snake are indicated by different colors and the trial number is labelled. The first number of the trial identification is the day of testing. The best performing glides are trial 618 from snake 95 and trial 505 from snake 88, which are shown in more detail in figure 7. (B) Overhead view of the glide path showing the unfiltered center of mass position in the inertial frame. The glides are generally not straight and show broad arcing behavior. (C) Velocity polar diagrams of forward and vertical velocity in the straightened frame. The glide angle is the angle subtended from the horizontal downward. (D) Velocity polar diagrams that have been non-dimensionalized and rescaled to remove the effects of animal size. Velocity trajectories show a characteristic vertical portion during the ballistic phase, followed by an upward arc onto the terminal velocity manifold near a rescaled velocity magnitude of 1. The lightest snake (snake 95) progresses farthest on the diagram and had the best glide performance (trial 618).



1614 **Fig. 5.** Center of mass acceleration and aerodynamic force estimates, nor-
1615 malized by body weight, as functions of height for three snakes that span
1616 the observed mass range of animals tested. The left column is determined
1617 from the right-hand side of equation (24) and consists of the experimental
1618 accelerations and gravity. The right column is determined from the left hand
1619 side of equation (24), which consists of the integrated lift and drag forces
1620 from the quasi-steady aerodynamic model. The black line is the average
1621 for all trials for each snake and the colored band is ± 1 standard deviation.
1622 (A) Lateral direction force and acceleration components are close to zero.
1623 (B) Forward forces, responsible for horizontal motion over the ground, are
1624 smoother than forward accelerations, but the force estimates are too low. (C)
Vertical forces, responsible for offsetting the animal's weight, are too high
compared to vertical accelerations. The dashed line (vertical force = 1) indi-
cates the equilibrium configuration when the aerodynamic forces balance the
weight (i.e., only gravity is acting on the snake in the vertical axis.).

1625
1626
1627
1628
1629
1630
1631
1632
1633
1634
1635
1636
1637
1638
1639
1640
1641
1642
1643
1644
1645
1646
1647
1648
1649
1650
1651
1652
1653
1654
1655
1656
1657
1658
1659
1660
1661
1662
1663
1664
1665
1666
1667
1668
1669
1670
1671
1672
1673
1674
1675
1676
1677
1678
1679
1680

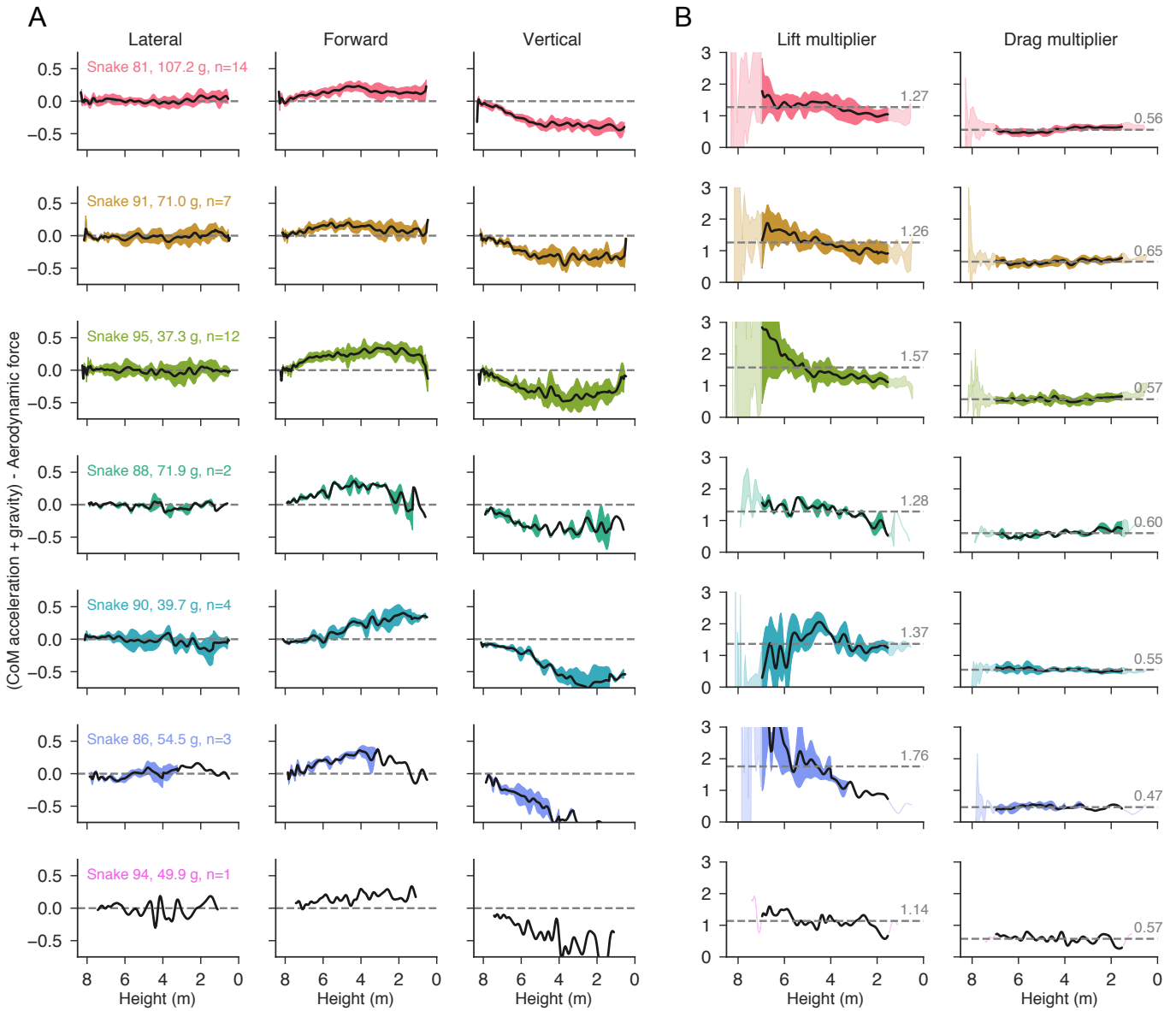
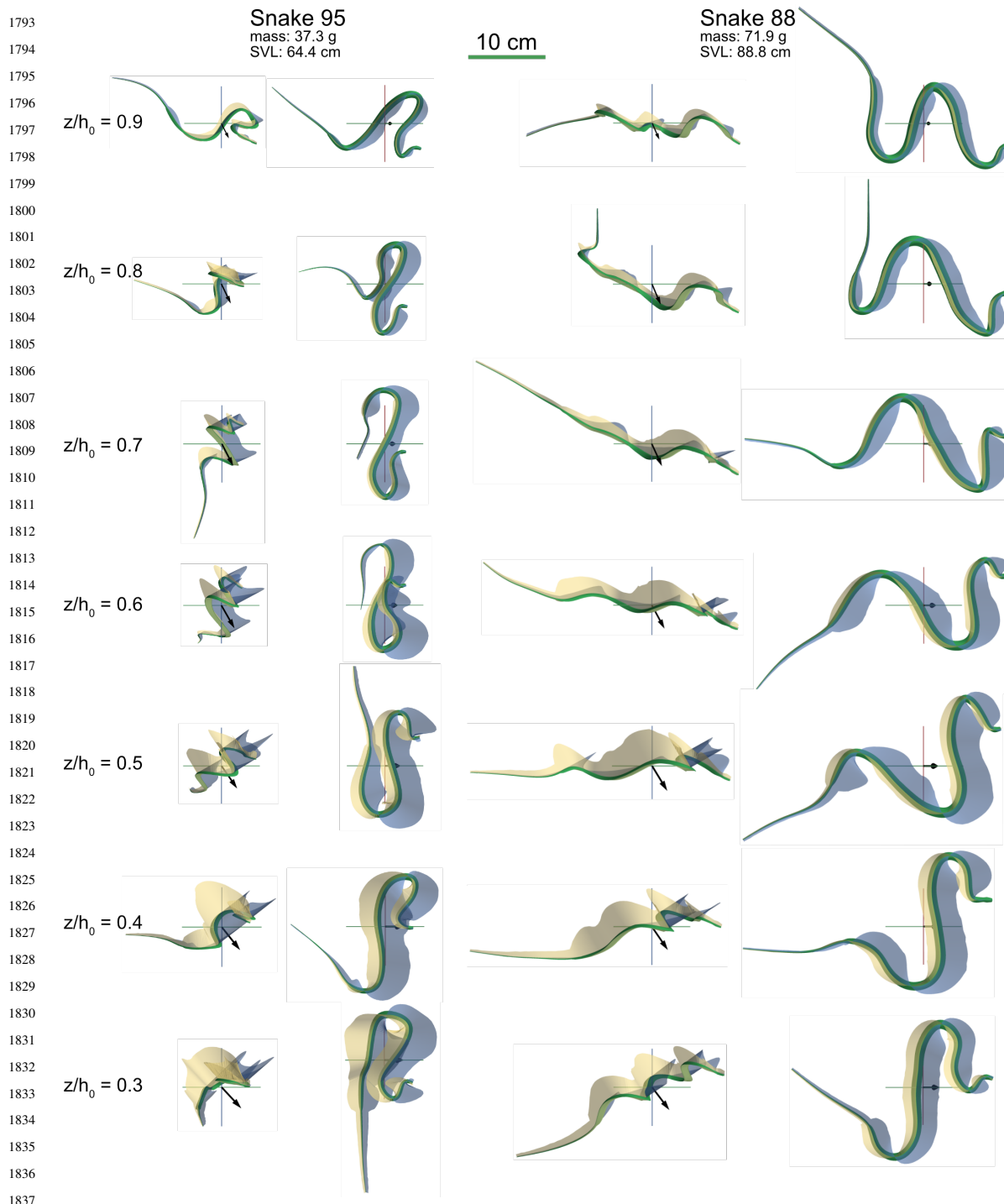


Fig. 6. Aerodynamic force errors and adjustments. (A) Absolute force errors normalized by body weight about the lateral, forward, and vertical directions given by equation (26) for 43 glide trials from seven snakes. The average errors are shown in black, with the colored bands indicating ± 1 standard deviation. Lateral errors are near zero. Forward force errors are positive, with a maximum error of 0.25 BW, indicating insufficient forward force. The vertical force error is negative, with a minimum of approximately -0.5 BW, indicating too much vertical force. (B) Adjustments to the quasi-steady lift and drag forces to reduce the forward and vertical force errors to zero. The left column is the multiplier needed for the lift force and the right column is the multiplier needed for the drag force. The drag multiplier is nearly constant for each glide and is approximately $0.6\times$, while the lift multiplier generally decreases throughout each glide. The average lift multiplier is approximately $1.35\times$.



1838 **Fig. 7.** Adjusted quasi-steady lift and drag force distributions for two snakes
1839 from the best performing glides; trail 618 from snake 95 on the left, and trial
1840 505 from snake 88 on the right; labeled as in figure 4. For each snake, lift
1841 force distribution (blue) and drag force distribution (yellow) are shown from
1842 the side and top view (left and right columns). Progress through the glide
1843 (height fraction) is marked by the rows, with 0.9 being closest to the launch
1844 branch. The instantaneous forces have been adjusted using the force multipliers
1845 from figure 6B. The instantaneous center of mass velocity is shown
1846 with the black arrow, and the center of mass location by the axes. Each image
1847 is scaled such that the green scale bar is 10 cm. The smaller snake, snake
1848 95, had more out-of-plane motion of the posterior body and a tighter body
1849 profile than the larger snake 88. For both animals, the drag force is continuous
1850 and large over the whole body, with the straight and 'U'-bend segments
1851 contributing similar amounts. The lift force is lowest at the 'U'-bends, but the
1852 symmetric airfoil produces force along the interior of the bend. The tail produces
1853 little force due to its small width.

1849
1850
1851
1852
1853
1854
1855
1856
1857
1858
1859
1860
1861
1862
1863
1864
1865
1866
1867
1868
1869
1870
1871
1872
1873
1874
1875
1876
1877
1878
1879
1880
1881
1882
1883
1884
1885
1886
1887
1888
1889
1890
1891
1892
1893
1894
1895
1896
1897
1898
1899
1900
1901
1902
1903
1904

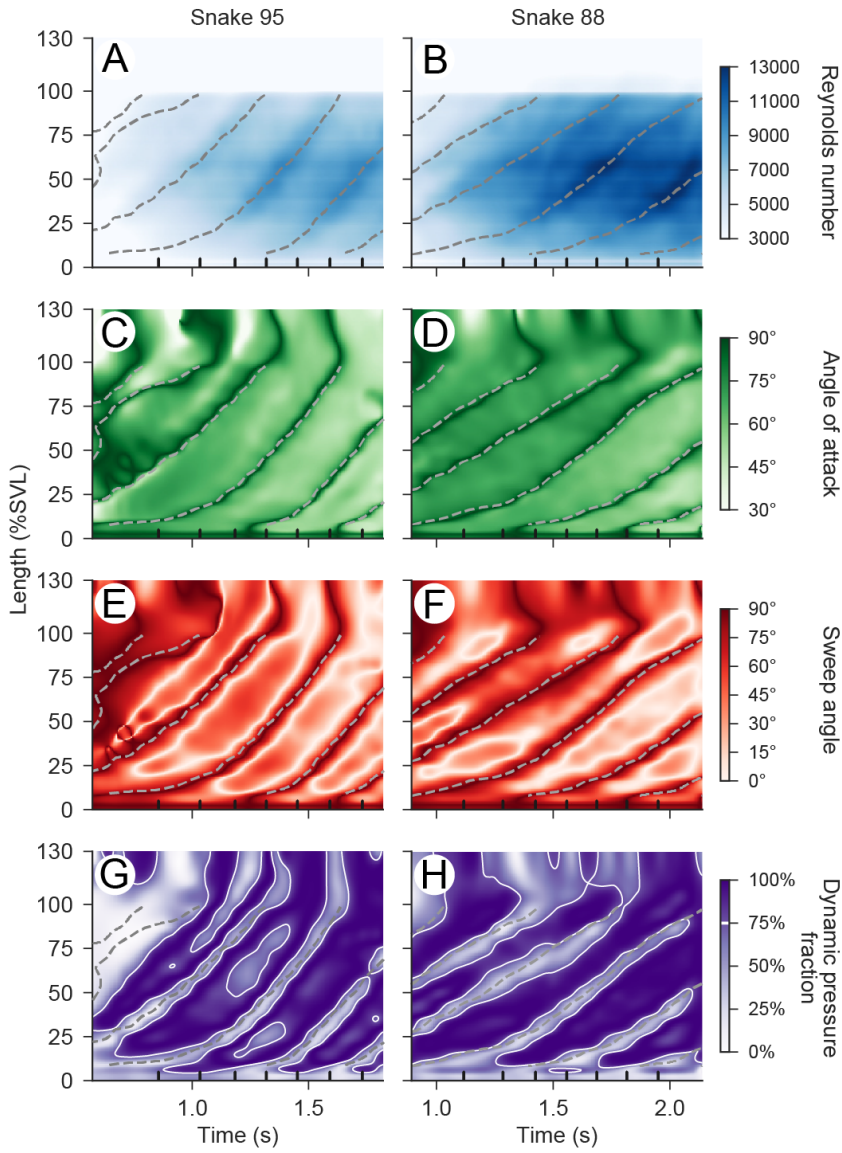


Fig. 8. Space-time plots of Reynolds number, angle of attack, sweep angle, and dynamic pressure fraction for the glides shown in figure 7. The locations of the time points in figure 7 are indicated by the vertical black marks along the abscissa. (A,B) Reynolds number distribution, where the gray dotted lines denote the 'U'-bends, found as zero crossings of the horizontal wave (Yeaton et al., 2020). The Reynolds number increases as the animal accelerates, with snake 88 having higher Reynolds numbers because it is wider than snake 95. The tail has a much lower Reynolds number because of its small width. (C,D) Angle-of-attack distributions, where the 'U'-bends are ridges of high angle of attack. (E,F) Sweep angle distribution, where ridges of high sweep at the 'U'-bends are surrounded by sweep angles near 0°. Both the angles of attack and sweep angles generally decrease as the glide shallows. (G,H) Fraction of the dynamic pressure, U_{\perp}^2/U^2 , due to simple sweep theory. Regions where over 75% of the dynamic pressure is maintained are dark and outlined with the white contour; these regions generally occur along the straight segments between the 'U'-bends.

1905
1906
1907
1908
1909
1910
1911
1912
1913
1914
1915
1916
1917
1918
1919
1920
1921
1922
1923
1924
1925
1926
1927
1928
1929
1930
1931
1932
1933
1934
1935
1936
1937
1938
1939
1940
1941
1942
1943
1944
1945
1946
1947
1948
1949
1950
1951
1952
1953
1954
1955
1956
1957
1958
1959
1960

1961
1962
1963
1964
1965
1966
1967
1968
1969
1970
1971
1972
1973
1974
1975
1976
1977
1978
1979
1980
1981
1982
1983
1984
1985
1986
1987
1988
1989
1990
1991
1992
1993
1994
1995
1996
1997
1998
1999
2000
2001
2002
2003
2004
2005
2006
2007
2008
2009
2010
2011
2012
2013
2014
2015
2016

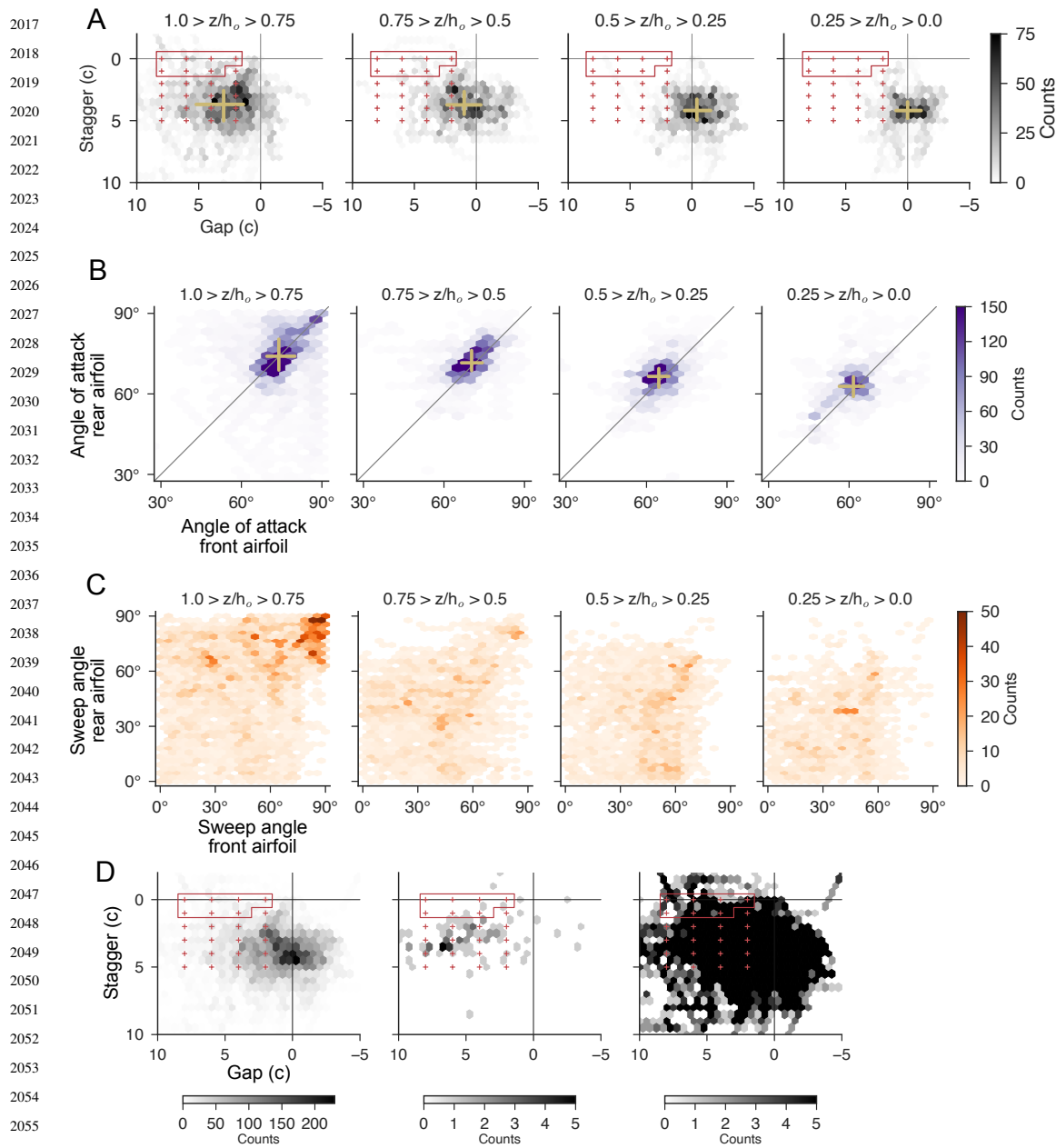


Fig. 9. Distributions of gap, stagger, angle of attack, and sweep angle of the 43 glide trials analyzed. Columns (A)–(C) show the distributions for different height fractions through the glide. (A) Distributions of stagger vs. gap, with the median, first, and third quartiles marked in yellow. The red '+' symbols denote measurement locations for wake interaction effects (Jafari et al., 2021). Measurement configurations where wake interaction effects are greatest are enclosed in the red box. Initially, the gap and stagger distributions are relatively disperse, but coalesce as the glides progress. (B) Angle of attack of the rear airfoil vs. angle of attack of the front airfoil. The angles of attack are correlated and initially spread along the diagonal. The angles of attack decrease as the glides progress, which results in more lift and less drag. (C) Sweep angle of the front and rear airfoils do not follow a clear trend, indicating the airflow is not usually perpendicular to the body, even along the straight segments. (D) Comparison of gap and stagger from this study (first panel) and from (Socha et al., 2010) (second panel). The third panel displays the same information as the first panel, but with the same color bar range as the second panel to highlight the spread of the data. The tandem effects test locations are overlaid on each plot. Each study has measured gaps and staggers in the wake interaction region.

Table 1. Summary of gap and stagger changes during different phases of gliding (figure 9A). The median and interquartile range (IQR) of gap (G) and stagger (S) are displayed in units of maximum chord length of the animal, denoted by “c”.

Height fraction	Median (G,S)	Gap IQR (Q1, Q3)	Stagger IQR (Q1, Q3)
$1.00 \geq z/h_0 \geq 0.75$	(3.0 c, 3.7 c)	3.8 c (1.4 c, 5.2 c)	2.4 c (2.6 c, 5.0 c)
$0.75 \geq z/h_0 \geq 0.50$	(1.0 c, 3.7 c)	2.7 c (-0.4 c, 2.4 c)	1.8 c (2.7 c, 4.5 c)
$0.50 \geq z/h_0 \geq 0.25$	(-0.4 c, 4.2 c)	2.1 c (-1.5 c, 0.6 c)	1.7 c (3.3 c, 5.0 c)
$0.25 \geq z/h_0 \geq 0.00$	(0.0 c, 4.2 c)	2.0 c (-1.1 c, 0.9 c)	1.3 c (3.5 c, 4.8 c)

2129
2130
2131
2132
2133
2134
2135
2136
2137
2138
2139
2140
2141
2142
2143
2144
2145
2146
2147
2148
2149
2150
2151
2152
2153
2154
2155
2156
2157
2158
2159
2160
2161
2162
2163
2164
2165
2166
2167
2168
2169
2170
2171
2172
2173
2174
2175
2176
2177
2178
2179
2180
2181
2182
2183
2184

2185
2186
2187
2188
2189
2190
2191
2192
2193
2194
2195
2196
2197
2198
2199
2200
2201
2202
2203
2204
2205
2206
2207
2208
2209
2210
2211
2212
2213
2214
2215
2216
2217
2218
2219
2220
2221
2222
2223
2224
2225
2226
2227
2228
2229
2230
2231
2232
2233
2234
2235
2236
2237
2238
2239
2240